Numerical Simulation of Three-Dimensional Unsteady Flow past Ice Crystals

PAO K. WANG AND WUSHENG JI

Department of Atmospheric and Oceanic Sciences, University of Wisconsin–Madison, Madison, Wisconsin

(Manuscript received 11 March 1996, in final form 14 February 1997)

ABSTRACT

The unsteady flow fields around falling columnar ice crystals, hexagonal ice plates, and broad-branch crystals are simulated by numerically solving the time-dependent Navier–Stokes equations appropriate for these geometries in the primitive equation form. A predictor–corrector method and a quadratic interpolation for convective kinematics (QUICK) scheme are applied on nonuniform grids to determine the velocity fields. The ice crystals are held in fixed orientation but time-dependent behaviors such as eddy shedding are allowed to occur by imposing an initial perturbation with a magnitude 30% of the free-stream velocity. The computed flow fields cover a Reynolds number range from 0.1 to about 200, being slightly different for different crystal habits. Examples of velocity fields are illustrated. The computed drag coefficients for cylinders agree with experimental values to within a few percent, while those for hexagonal plates agree with experimental values and previous calculations by Pitter et al. to less than 15% even though the aspect ratios are different. The drag coefficients for broad-branch crystals are higher than those for hexagonal plates at the same Reynolds numbers. Special features of flow passing through the branch gaps of broad-branch crystals suggest that it may be possible to use a creeping flow assumption to treat flow passing through spaces in complicated dendritic crystals.

1. Introduction

Any quantitative investigation of the formation of clouds and precipitation cannot avoid dealing with the complicated motion of particles such as cloud droplets, raindrops, ice crystals, graupel, and hailstones. These particles move in a viscous medium, the air, and thus create complicated flow fields around themselves. These fields have important effects on the growth of the particles themselves. For example, due to the existence of these flow fields, the collision efficiencies of two spherical drops can be significantly different from one that would have been the case if the two spheres are colliding in a vacuum due to pure inertial collision. The same can be said for any pairs of cloud and precipitation particles. Since the collisional growth is a very important mechanism responsible for the precipitation particle formation, especially in the warm rain process, it goes without saying that the flow fields have significant impact on both the time and magnitude of the precipitation development.

But the knowledge of flow fields is important even for the growth of small cloud particles. These particles have relatively small collision efficiency with each other, and their growth is mainly achieved by the diffusion of ambient water vapor toward them. The flow fields created by their motion influence the vapor density gradients, which, in turn, determine the diffusional growth rates of these particles. The amount of the influence, called the ventilation factor, is strongly controlled by the flow field associated with the falling particle (Pruppacher and Klett 1978, chapter 13). This factor is also important in determining the evaporation rates and the surface temperatures of large falling hydrometeors, although their growth rates depend also on the collisional process.

In principle, the flow fields can be obtained either by experimental measurements or theoretical calculations. Experimental methods are preferred if feasible and if they can be done properly. The reality is, however, that it is very difficult to measure the flow fields for a wide variety of cloud and precipitation particles, which vary greatly in size and shape, and for a wide range of atmospheric conditions. The other option is to perform theoretical calculations to see if the calculations can be done based on realistic models and if they can be done efficiently. The advent of fast computers makes this option a viable choice and the calculations can often be done at a relatively economic cost compared to experimental measurements. The present study is based on the theoretical approach.

2. Review of previous studies

Most of the previous work on the theoretical studies of hydrodynamics relevant to cloud and precipitation

Corresponding author address: Dr. Pao K. Wang, Department of Atmospheric and Oceanic Sciences, University of Wisconsin–Madison, 1225 W. Dayton Street, Madison, WI 53706.
E-mail: pao@windy.meteor.wisc.edu

particles has been reviewed and summarized by Pruppacher and Klett (1978) and Clift et al. (1978). Among the earlier work relevant to this area are the analytical and semi-empirical studies of Stokes (e.g., Happel and Brenner 1965; Yih 1969), Goldstein (1929), and Carrier (1953) regarding flow past rigid spheres, and Hadamard (1911) and Rybczinski (1911, see Lamb 1945) regarding fluid spheres. Refinements of these early studies were made by many fluid dynamicists that are too numerous to cite here. However, it was soon realized that these analytical solutions can only be applied to a limited range of real atmospheric conditions; in order to produce results that are useful to cloud physics, it is necessary to prescribe initial and/or boundary conditions that are more complicated and closer to realistic cloud environment. It would be very difficult to solve these problems analytically, and indeed they are most conveniently solved by numerical methods. Thus, Jenson (1959), Le Clair et al. (1970), and Pruppacher et al. (1970) started to perform numerical calculations of fields for incompressible flow past rigid and liquid spheres.

Spherical problems, especially those of low Reynolds number range, are largely relevant only to cloud drops. The majority of other cloud and precipitation particles are prominently nonspherical. Large raindrops have relatively flat bottoms and round tops that resemble hamburger buns. Columnar ice crystals, dendrites, and conical graupel are certainly far from being spherical. There is clearly a need to determine the flow fields around nonspherical hydrometeors. A few cases of these have been carried out by some investigators. Again, more realistic solutions were obtained mainly by numerical methods. For instance, the flow past infinitely long cylinders, which are often used to approximate flow fields around ice columns, were obtained by numerous researchers (e.g., Thom 1933; Dennis and Chang 1969, 1970; Hamielec and Raal 1969; Takami and Keller 1969; Schlamp et al. 1975.) The numerical flow fields around thin oblate spheroids, used to approximate hexagonal ice plates, were obtained by Rimon and Lugt (1969), Masliyah and Epstein (1970), and Pitter et al. (1973).

All the studies mentioned above have two things in common: First, they all treated steady-state flow fields, which are only applicable to motion of cloud and precipitation particles at low Reynolds numbers, and second, they treated only two-dimensional problems. In that Reynolds number range, the particles fall steadily and therefore the flow fields around them are also independent of time. However, when these particles grow larger, they start to show unsteady fall behavior and create unsteady flow fields characterized first by the shedding of eddies in the downstream and then by the eventual turbulent eddies when the Reynolds numbers become sufficiently large. Undoubtedly, if we are to understand the unsteady motion of these particles and their effect on the cloud growth, we need to determine these unsteady flow fields. This amounts to solving the unsteady Navier–Stokes equations with appropriate initial and boundary conditions. In addition, the flow fields around most real ice crystals are actually three-dimensional in nature even when the flow is steady. For example, the steady flow past a hexagonal plate does not really possess azimuthal symmetry as would be the case for a circular disk or a thin oblate spheroid. The flow past a cylinder of finite length is even more asymmetrical due to the presence of a cylindrical surface and two plain end surfaces. When the flow becomes unsteady, of course, the asymmetry becomes even more pronounced.

We have recently developed some numerical techniques and used them to compute the flow fields around a few types of nonspherical ice particles in the low–medium (from 0.1 to about 150) Reynolds number range. The results appear to be very encouraging. We believe that the same techniques can be extended to more complicated cases. Some preliminary results of our computation have been reported recently (Ji and Wang 1990, 1991). This paper presents more complete results and the intercomparison of the results between the flow fields of different particles. We have also used the computed flow fields of these ice particles to determine their collisional and diffusional growth rates and the results will be reported elsewhere.

3. The physics and mathematics of unsteady flow fields around nonspherical ice particles

a. Streamfunction versus momentum equation formulation

In this section, we shall discuss the conceptual setup of the problems for unsteady flow past nonspherical ice crystals and the numerical schemes that we used to solve them. In the treatment of two-dimensional steady-state incompressible flow problems, it is common to formulate the problems in terms of a scalar streamfunction ψ. The benefit of doing so is that only a single dependent scalar variable needs to be solved and the components (e.g., u, v) of the flow velocity vector $\mathbf{V}$ can be derived from ψ. On the other hand, using the original momentum equation formulation would require solving two dependent variables.

Unfortunately, the attractiveness of the streamfunction formulation disappears for three-dimensional flows. While it is still possible to define a streamfunction, this function will be a vector instead of a scalar one (e.g., Anderson et al. 1984). This means that three separate component equations of the streamfunction need to be solved instead of one. Thus there is no advantage to the streamfunction formulation over the original momentum equations. In the present study, the momentum equation formulation is used.

b. The incompressible Navier–Stokes equations and the initial and boundary conditions

We shall treat three relatively simple ice crystal shapes, namely, the columnar ice crystals (approximated

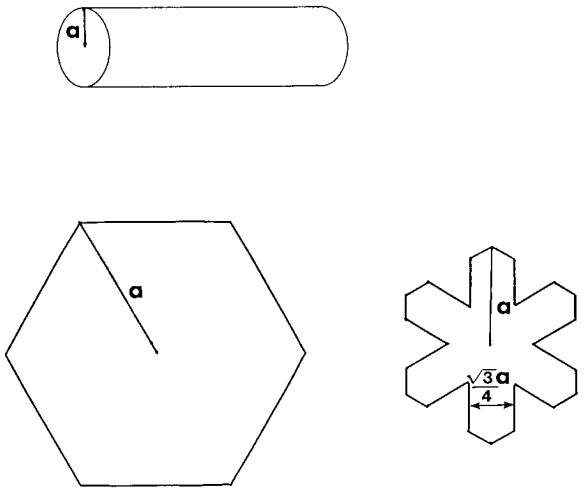

FIG. 1. The three types of ice crystals considered in this study.

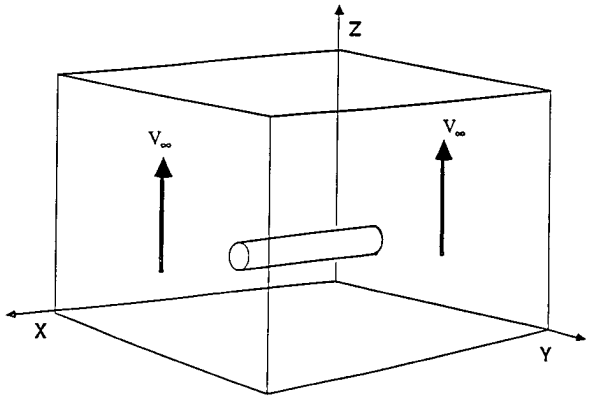

FIG. 2. The general configuration of the theoretical problem. Ice crystals are assumed to fall with their long axes in the horizontal direction.

by finite circular cylinders), hexagonal ice plates, and broad-branch crystals. Figure 1 shows a schematic sketch of these three types of crystals. The quantity a represents the ''radius'' of the ice crystals as defined in the figure. We shall also assume that these ice crystals fall with their broad dimensions oriented in the horizontal direction, which is known to be the common fall orientation of many medium-sized ice crystals (Pruppacher and Klett 1978). It is known that large ice crystals also exhibit zigzag fall attitude, but this is not simulated here due to the limitation of computer resource. The schematic configuration of the theoretical problem considered here is shown in Fig. 2.

To facilitate the numerical analysis, we first introduce the dimensionless variables

$$x' = \frac{x}{a}, \qquad \mathbf{V}' = \frac{\mathbf{V}}{|\mathbf{V}_\infty|}, \qquad t' = \frac{t|\mathbf{V}_\infty|}{a},$$

$$P' = \frac{P}{\rho|\mathbf{V}_\infty|^2}, \qquad \mathrm{Re} = \frac{2|\mathbf{V}_\infty|a}{\nu}, \tag{1}$$

where x (or y, z) is one of three Cartesian coordinates, $\mathbf{V}$ is the fluid velocity, $\mathbf{V}_\infty$ the free-stream velocity equal to the terminal fall velocity of the ice crystal, P the dynamic pressure, and ν the kinematic viscosity of the fluid. Here, Re is the Reynolds number relevant to the flow. All primed quantities are nondimensional. Using these dimensionless variables, we can write down the nondimensional Navier–Stokes equation and the continuity equation as (after dropping the primes)

$$\frac{\partial \mathbf{V}}{\partial t} + \mathbf{V}\cdot\nabla\mathbf{V} = -\nabla P + \frac{2}{\mathrm{Re}}\nabla^2\mathbf{V}, \tag{2}$$

$$\nabla\cdot\mathbf{V} = 0. \tag{3}$$

The ideal boundary conditions appropriate for the present problems are

$$\mathbf{V} = 0 \quad \text{at the surface of the ice crystal, and} \tag{4}$$

$$\mathbf{V} = \mathbf{1}\cdot\mathbf{e}_z \quad \text{at infinity,} \tag{5}$$

where $\mathbf{e}_z$ is the unit vector in the general flow direction. In real numerical computations, of course, the domain is always finite and the condition (5) can only be taken to mean that the velocity is constant at an outer boundary that is sufficiently far away from the crystal. It is difficult at present to determine from purely theoretical grounds how far the distance should be in order to be ''sufficiently far.'' We did this by trial and error, and the outer boundary is considered far enough when the computed results do not change within a few percents as we move the boundary out. Similar treatment was

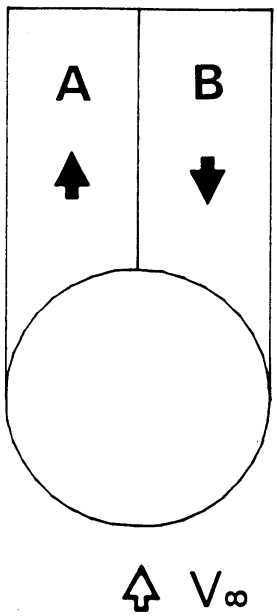

FIG. 3. The initial perturbation imposed on the steady flow field in order to generate time-dependent flow behavior. The magnitude of perturbation in region A and B is 30% of the free-stream velocity, but the directions of the perturbations are opposite.

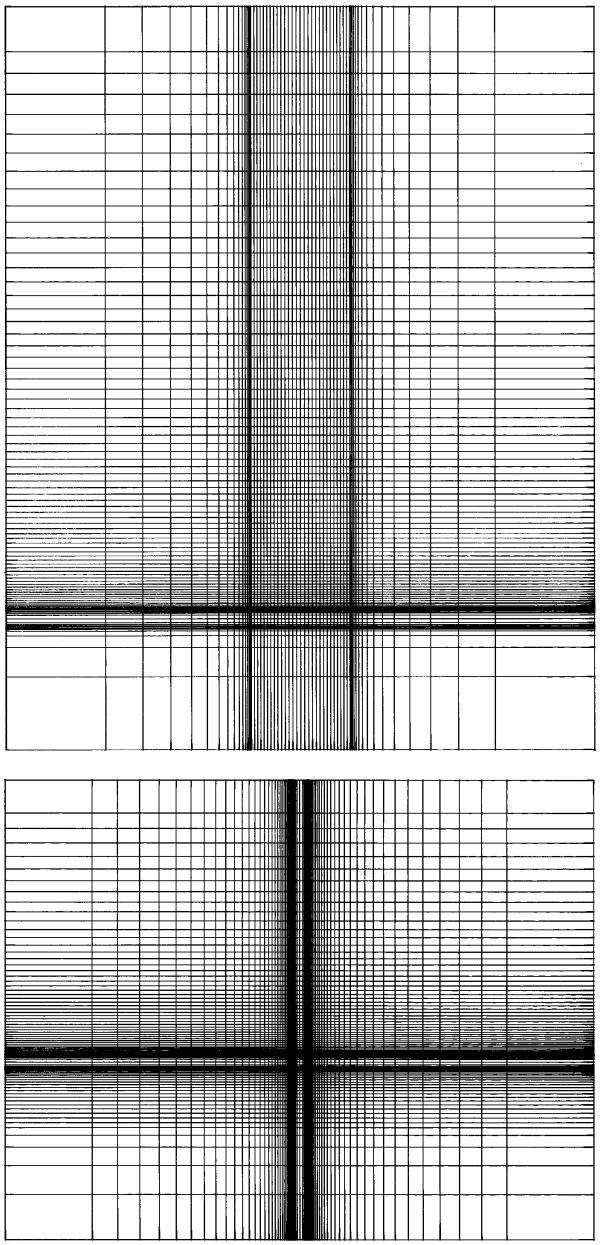

FIG. 4. The nonuniform grid used for numerically solving the Navier–Stokes equations for flow past a columnar ice crystal. (a) Broadside view. (b) End view.

done for all outer boundaries. Table 1 shows the locations of the upstream, downstream, and lateral boundaries for determining the numerical flow fields for the three cases.

While condition (5) is approximately valid in the upstream and lateral boundaries, it is usually not valid in the downstream boundaries. This is due to the fact that at higher Reynolds number ranges as investigated here, the shedding of eddies may occur. The disturbances often propagate downstream for a long distance. Thus the condition at the downstream boundary is replaced by a weaker condition, $\partial \mathbf{V}/\partial z = 0$.

TABLE 1. Outer boundaries of the computational domains for the three crystal cases. The radius is 1.

Boundaries	Columnar crystal	Hexagonal plate	Broad-branch crystal
Upstream	12.7	3.3	1.7
Lateral (lengthwise)	25.5	6.74	10.10
(end-on)	23.5	6.86	11.09
Downstream	63.0	14.3	15.27

The pressure field can be determined from the Navier–Stokes equation at all boundaries except at the downstream boundary where the condition $\partial P/\partial z = 0$ is used. Since we are dealing with unsteady flow here, we also need initial conditions to close the equations. The initial conditions are $P = 0$ and $\mathbf{V} = \mathbf{1}\cdot\mathbf{e}_z$ everywhere at $t = 0$ except at the surface of the crystal. The condition on the surface is $\mathbf{V} = 0$ (nonslip condition) at all t.

c. Generation of unsteady flow features

Although the Navier–Stokes equation (2) is written as a time-dependent equation, this does not mean that the computational results will always result in time-dependent flow features such as the shedding of eddies. Indeed, Dennis and Chang (1970) has shown that for flow past two-dimensional cylinders starting with symmetric initial conditions, the eddy shedding does not occur even at high Reynolds numbers. In order to generate these time-dependent, or unsteady, features, it is necessary to implement an asymmetric initial perturbation field. There are many ways of implementing this perturbation. For example, Braza et al. (1986) achieved this on a two-dimensional cylinder by performing a rotation of the cylinder along its axis. In the present study, we achieve this by implementing a velocity perturbation of magnitude $0.3\mathbf{V}_\infty$ in the downstream region immediately behind the crystal to the steady-state solutions as shown in Fig. 3. The directions of the perturbation are opposite to each other in regions A and B, so as to form a shear along the central plane of the flow. As we shall see later, at high enough Reynolds numbers, this perturbation will generate a periodic eddy-shedding pattern in the simulated flow. On the other hand, the perturbation will be damped out in a short time if the Reynolds number is low.

4. The numerical scheme

To solve Eqs. (2) and (3) with the appropriate initial and boundary conditions, we adopt a numerical approach utilizing the finite difference method. It is also necessary to set up a mesh grid. Due to the more complicated shapes of these ice crystals, it is decided that the simplest way to set up grids is to use the Cartesian

TABLE 2. Dimensions of columnar ice crystals treated in the present study. Units: dimensionless.

Re	Diameter (d)	Length (L)	$\frac{L}{d}$
0.2	2.0	2.85	1.43
0.5	2.0	2.85	1.43
0.7	2.0	3.08	1.54
1.0	2.0	3.33	1.67
2.0	2.0	4.44	2.22
5.0	2.0	6.67	3.33
10.0	2.0	10.00	5.00
20.0	2.0	16.67	8.33
40.0	2.0	12.58	6.29
70.0	2.0	25.32	12.66

TABLE 3. Dimensions of hexagonal ice plates treated in the present study. Units: dimensionless.

Re	Diameter (d)	Thickness (h)	$\frac{h}{d}$
1.0	2.0	0.225	0.1125
2.0	2.0	0.177	0.0885
10.0	2.0	0.1265	0.06325
20.0	2.0	0.1034	0.0517
35.0	2.0	0.0863	0.04315
60.0	2.0	0.0725	0.03625
90.0	2.0	0.064	0.032
120.0	2.0	0.0576	0.0288

coordinate system. In order to prescribe the inner boundary conditions with adequate precision, the grid spacing near the crystal surface has to be small. On the other hand, the grid spacing far from the crystal can be larger to save computing time. This results in nonuniform grids used in the present study, as shown in Fig. 4.

As indicated before, the primitive velocity formulation of the Navier–Stokes equation is adopted for this study. The velocity at each time step is obtained by a predictor–corrector method. First, the velocity predictor $\mathbf{V}^*$ is determined by solving the equation

$$\frac{\mathbf{V}^* - \mathbf{V}^n}{\Delta t} + (\mathbf{V}^n \cdot \boldsymbol{\nabla})\mathbf{V}^n = \frac{2}{\mathrm{Re}} \nabla^2 \mathbf{V}^n, \tag{6}$$

where $\mathbf{V}^n$ is the velocity solved at time step n and Δt is the time increment. The pressure at time step $n + 1$ is then given by

$$\nabla^2 P^{n+1} = \frac{\boldsymbol{\nabla} \cdot \mathbf{V}^*}{\Delta t} \tag{7}$$

(e.g., Peyret and Taylor 1983). Finally, the velocity at time step $n + 1$ is determined by

$$\frac{\mathbf{V}^{n+1} - \mathbf{V}^*}{\Delta t} = -\boldsymbol{\nabla} P^{n+1}. \tag{8}$$

The scheme of velocity interpolation at each time step is the modified QUICK (Quadratic Upstream Interpolation for Convective Kinematics) scheme with second order accuracy developed by Leonard (1979) and extended by Davis (1984) and Freitas et al. (1985). Since we use the nonuniform mesh grid here, the uniform grid formulation given by Leonard (1979) cannot be used. Instead, we adopted the formulation of Freitas et al. (1985) for nonuniform grid but modified to suit our three-dimensional flow cases. The details of the formulation and the stability criterion are given in Ji and Wang (1990, 1991).

The Poisson equation for pressure, Eq. (7), is solved by the standard successive over-relaxation (SOR) method as described in Peyret and Taylor (1983) and Anderson et al. (1984).

The time step Δt used in the integration varies from 0.015 to 0.03, depending on the local grid spacing, such that the stability criterion is satisfied. The smallest grid spacing was Δx equals 0.0775. The largest grid size used was $59 \times 75 \times 89$. Naturally, a larger grid size will result in better accuracy but will increase the computing time considerably. The typical computing time for 10 000 time steps is on the order of a few hours on a CRAY X/MP computer. The computation on a CRAY-2 computer is somewhat faster. It appears that the SOR scheme in solving the pressure equation is the main bottleneck of the computation. The grid size used in this study represents a compromise between accuracy and available computing resources.

5. Results and discussion

The size, aspect ratios, and Reynolds numbers of the columns, hexagonal plates, and broad-branch crystals are listed in Tables 2, 3, and 4, respectively. Their dimensions are chosen to overlap those adopted by some previous work (Schlamp et al. 1975; Pitter et al. 1973, 1974; Pitter 1977; Miller and Wang 1989) so that the results can be compared. In the following we shall discuss the results for each crystal type separately.

a. General features of the flow fields around falling columnar ice crystals

As mentioned earlier, this type of crystal is approximated by a circular cylinder of finite length. Because of the finite length, the cylinder, as well as the flow field

TABLE 4. Dimensions of broad-branch crystals treated in the present study. Units: dimensionless.

Re	Diameter (d)	Thickness (h)	$\frac{h}{d}$
1.0	2.0	0.15	0.075
2.0	2.0	0.14	0.07
10.0	2.0	0.0914	0.0457
20.0	2.0	0.080	0.040
35.0	2.0	0.0667	0.033
60.0	2.0	0.060	0.030
90.0	2.0	0.052	0.026
120.0	2.0	0.047	0.0235

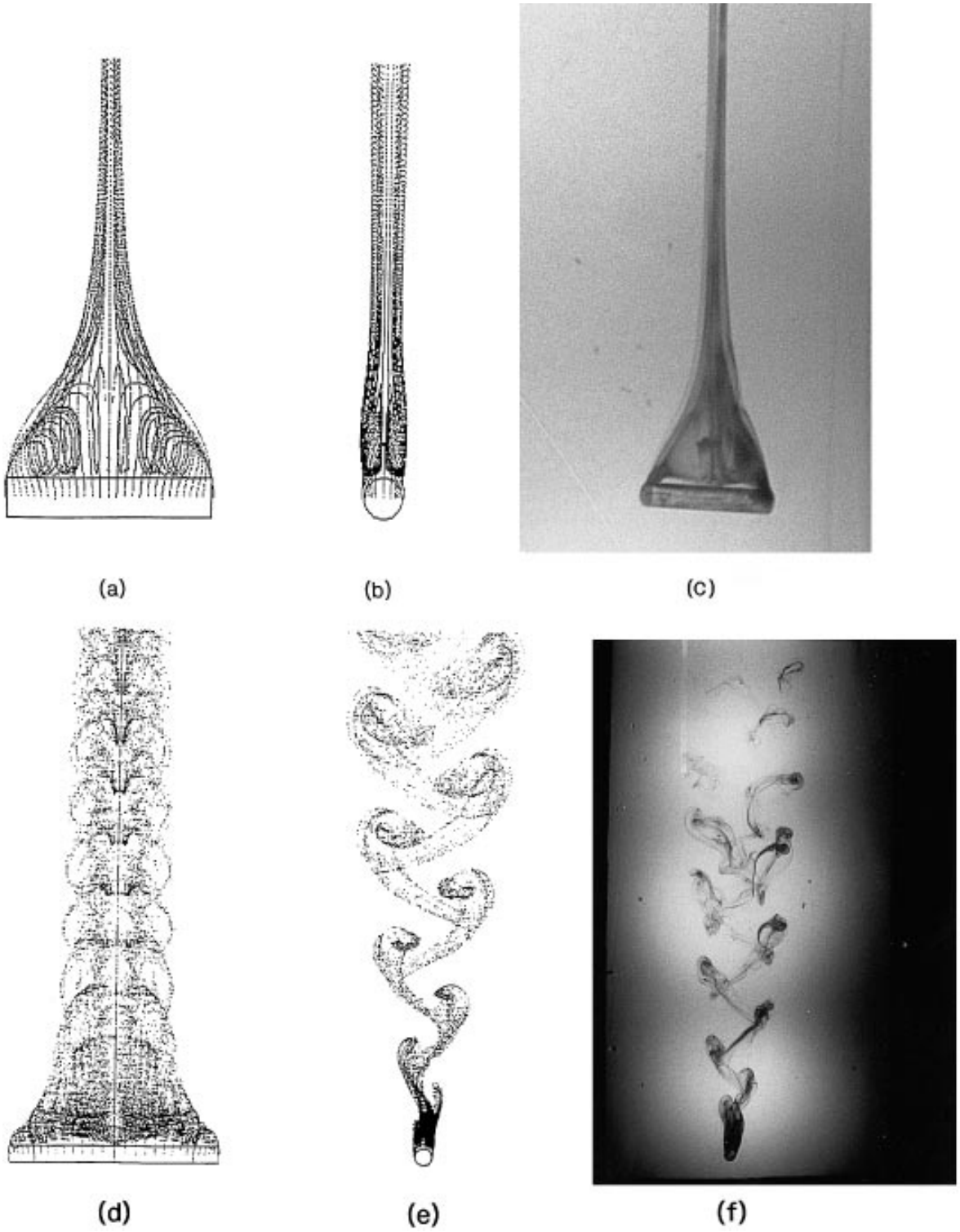

FIG. 5. Streak pattern, or ''snapshot'' field, of massless tracer particles for flow past an ice column. (a) Broad-side view, Re = 40. (b) End view, Re = 40. (c) Experimental photograph of a falling short cylinder at Re = 40. (d) Broad-side view, Re = 70. (e) End view, Re = 70. (f) Experimental photograph of a falling short cylinder at Re = 70 (photo courtesy of Dr. K. O. L. F. Jayaweera).

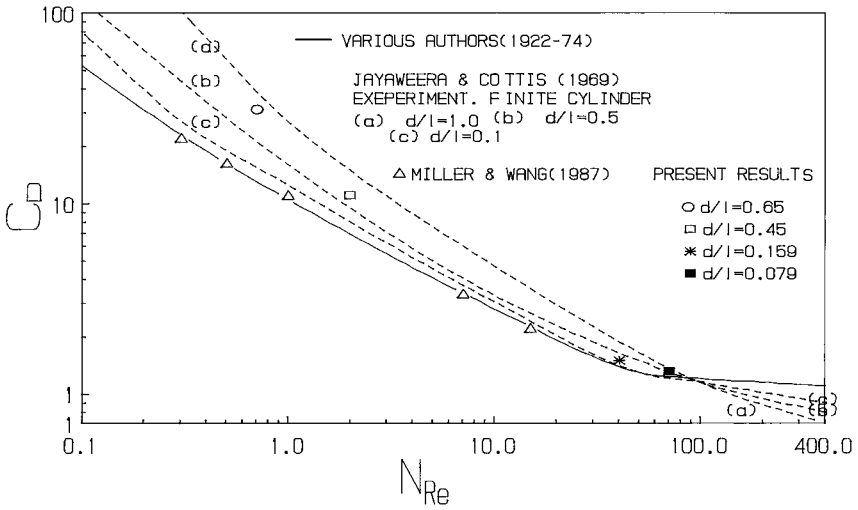

FIG. 6. Drag coefficients for flow past cylinders of various *d*/*l* ratios. The solid line and the triangles are for infinitely long cylinders. It is seen that as the Re increases, the cylinder becomes longer and the drag coefficient becomes closer to that of the infinitely long cylinder.

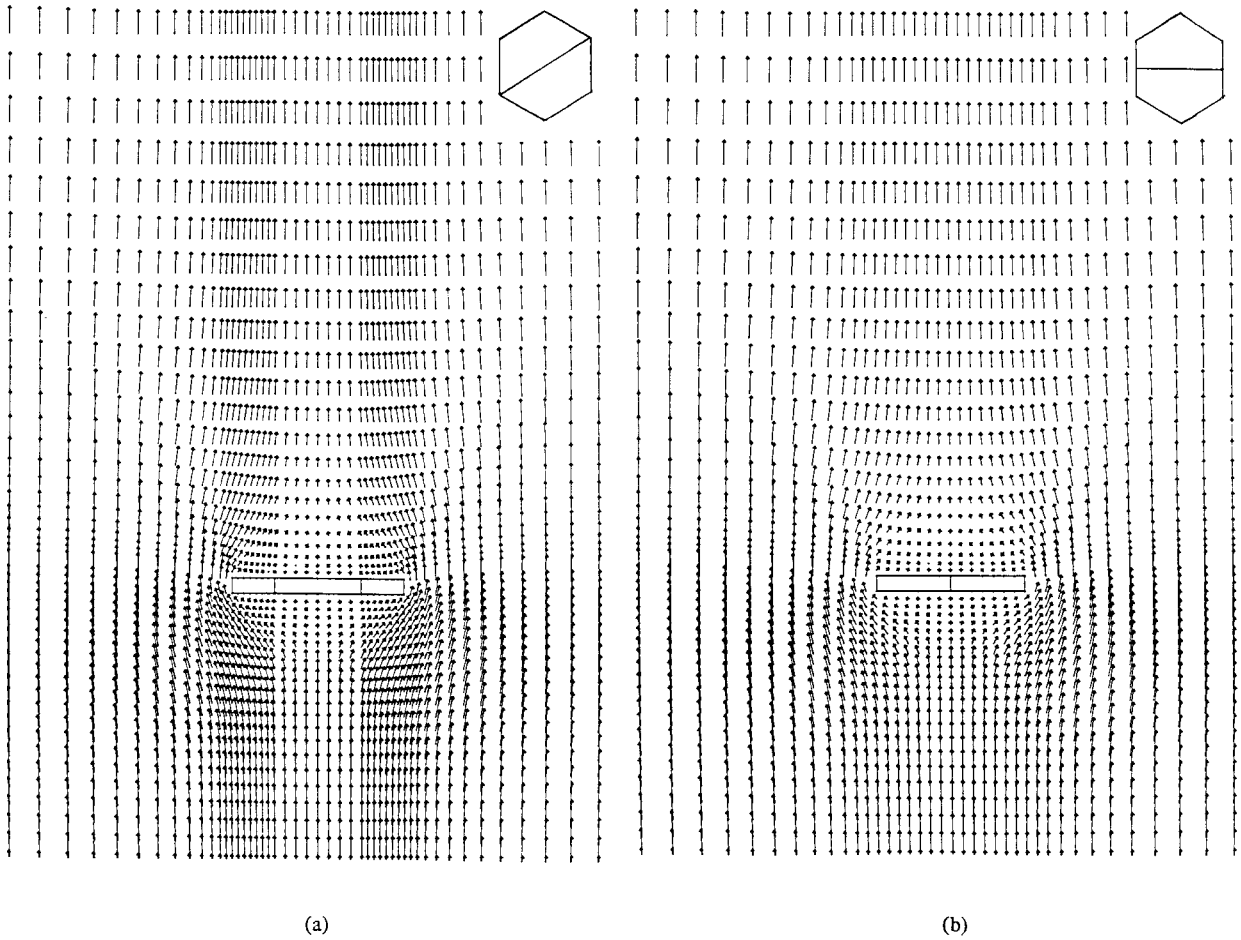

(a) (b)

FIG. 7. Velocity fields of flow past a hexagonal ice plate at Re = 2. The cross-section location is indicated by the dashed line in the upper right corner of the figures. Vectors represent projections of the 3D vectors onto that cross-sectional plane.

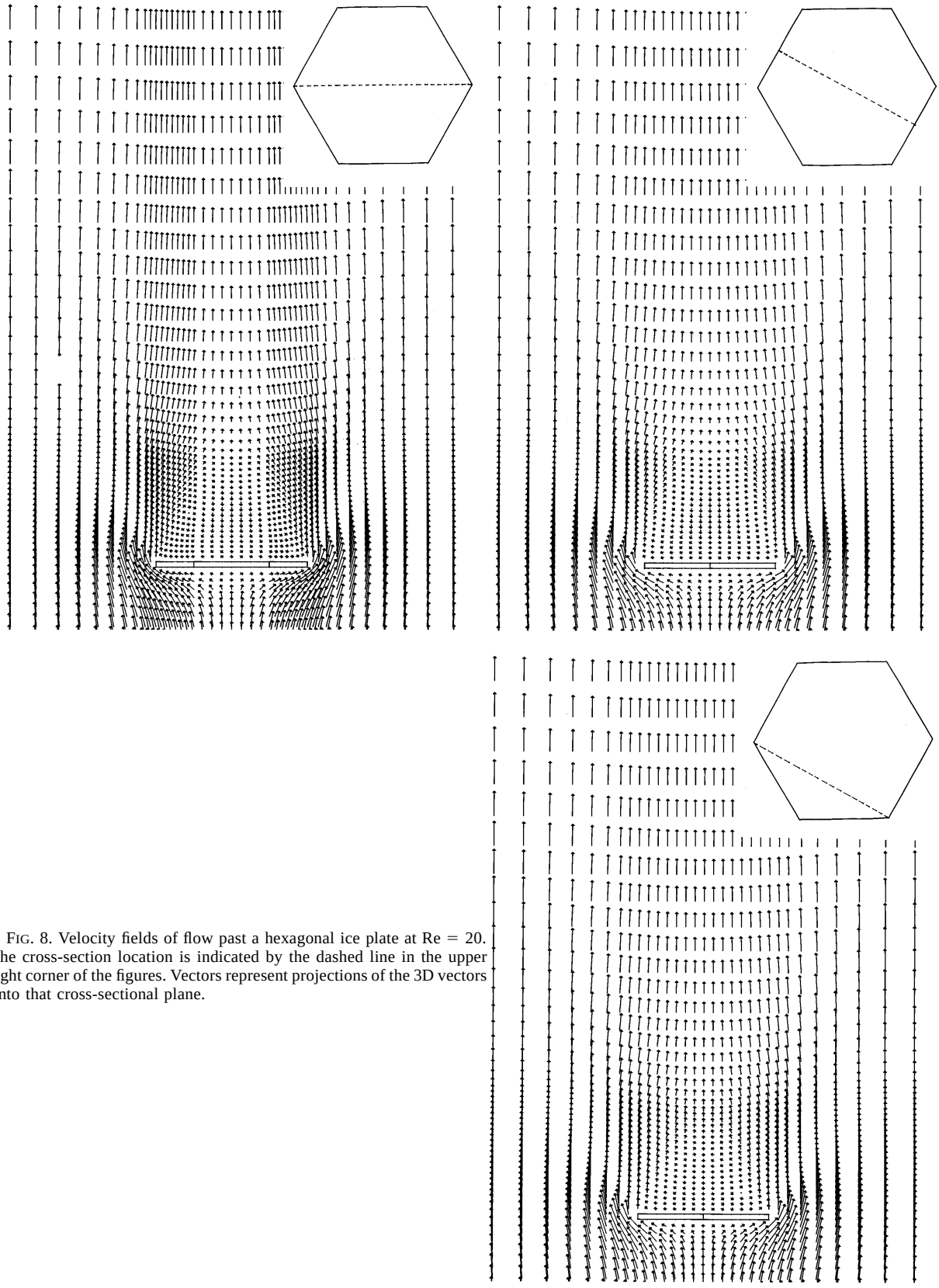

FIG. 8. Velocity fields of flow past a hexagonal ice plate at Re = 20. The cross-section location is indicated by the dashed line in the upper right corner of the figures. Vectors represent projections of the 3D vectors onto that cross-sectional plane.

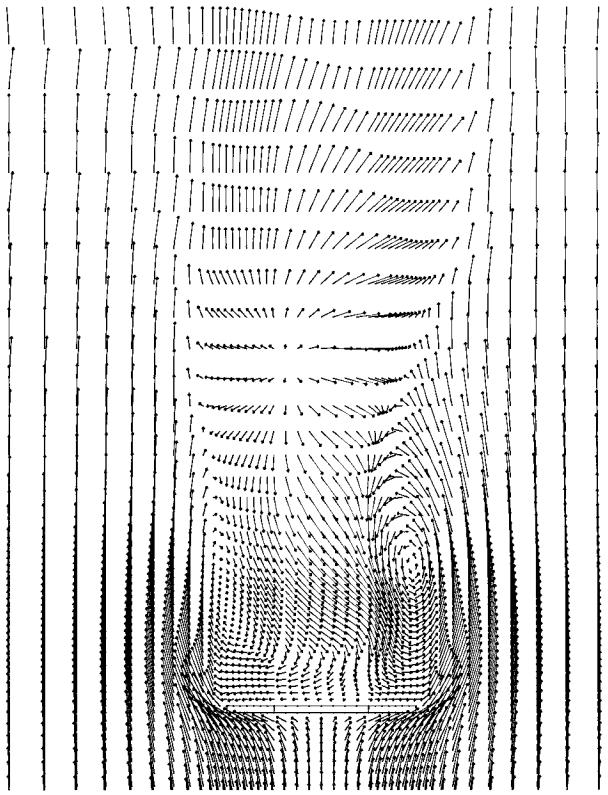

FIG. 9. The unsteady flow field past a hexagonal ice plate at Re = 140.

around it, is no longer cylindrically symmetric. The dimensions and aspect ratios of the cylinders chosen for the computation are shown in Table 2 and are the same as those given by Schlamp et al. (1975) for Reynolds numbers between 0.2 and 20, and by Jayaweera and Mason (1965) for Reynolds numbers 40 and 70. Several higher Reynolds numbers cases were also computed for the purpose of checking, but the details of these will not be discussed here. The aspect ratios of the cylinders specified by Schlamp et al. (1975) are taken from the actual samples whose diameter-length relations were reported by Auer and Veal (1970). For the higher Reynolds number cases, the Jayaweera and Mason's (1965) cylinder dimensions are also used here because their results are the only experimental data available for verification purpose for free-falling finite cylinders. In all cases, the ice columns become longer as compared to the diameters as the Reynolds number increases.

Previous experimental studies of both two- and three-dimensional flow past circular cylinders indicated that the flow remains steady up to Re $\approx$ 50 (e.g., Kovasznay 1949; Jayaweera and Mason 1965). In Ji and Wang (1990, 1991), it was shown that even with the $0.3\mathbf{V}_\infty$ perturbation, the periodic shedding of eddies did not develop in the simulated flow field when Re = 40. Instead, it just produced a transient disturbance that quickly dissipated in about 45 time steps. On the other hand, when the Reynolds number increases to 70, the flow past the same cylinder developed a full-fledged periodic eddy shedding. This indicates that the current scheme is capable of simulating the eddy shedding phenomenon correctly. Thus no perturbation was necessary for computing the flow fields with Re $\leq$ 50.

Since many of the features of the flow past finite cylinders have been discussed in one of our previous papers (Ji and Wang 1991), only a brief summary and some highlights are given here. It is sufficient to say that the numerical results reproduced the features of flow fields observed in the laboratory experiments of Jayaweera and Mason (1965), such as the pyramidal wake region for Re $\leq$ 40 and the shedding of eddies for flow in greater Reynolds number range. Figure 5 gives a pictorial comparison between the computed massless tracer streaks and experimental photographs of Jayaweera and Mason (1965). It is seen here that there are good similarities between the two sets of pictures.

Figure 6 shows the comparison between the computed drag coefficients with those obtained by other theoretical and experimental results. The drag coefficient is defined as

$$C_D = \frac{D}{\rho V_\infty^2 \alpha}, \tag{9}$$

where D is the drag force and α is one-half of the cross-sectional area of the cylinder normal to the flow direction. Obviously, the drag coefficients of the present results differ from the results for infinite long cylinders. The difference is greater for smaller Reynolds number. This is due to the fact that the dimensions of columns for lower Reynolds numbers are such that their shapes differ more from an infinitely long cylinder. On the other hand, columns for higher Reynolds numbers are closer to the shape of an infinitely long cylinders, hence their drag coefficients are closer to each other. This implies that the theoretical results obtained by previous investigators regarding the behavior of columnar ice crystals are probably reasonable for the case of larger ice columns but not for short columns. The collection efficiencies of small droplets by columns and ventilation factors of falling ice columns computed based on our new scheme did show such trends and will be reported elsewhere. The discrepancies exist mainly for Re $<$ 10. It is seen here that the coefficients are practically the same as that of infinitely long cylinders for Reynolds number $>$ 10. The drag coefficients calculated here can be fitted by the expression

$$\log_{10} C_D = 2.44389 - 4.21639A - 0.20098A^2 + 2.32216A^3, \tag{10}$$

where

$$A = \frac{\log_{10}\mathrm{Re} + 1.0}{3.60206}. \tag{11}$$

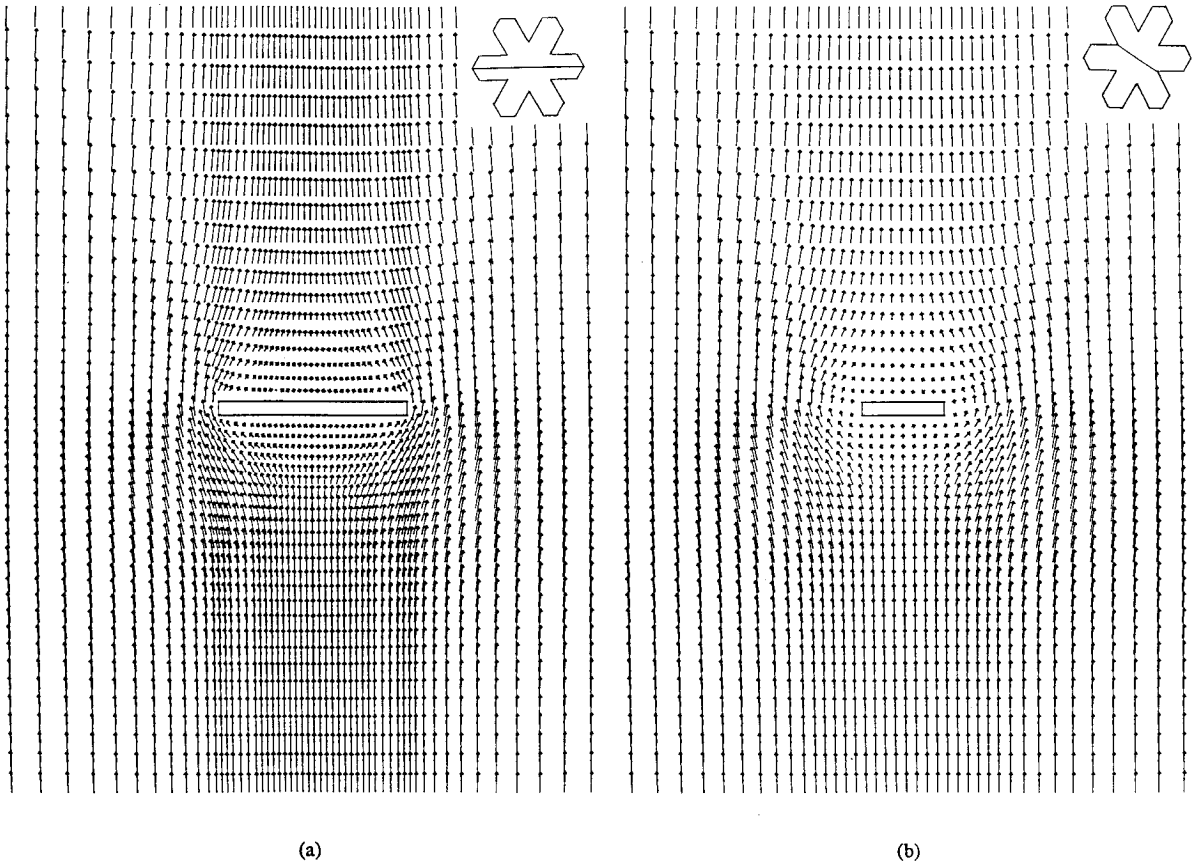

FIG. 10. Velocity fields of flow past a broad-branch ice crystal at Re = 2. The cross-section location is indicated by the dashed line in the upper right corner of the figure.

This formula is valid within the range $0.2 < \mathrm{Re} < 100$. It fits the computed data to within a few percent. Note that in reality the drag coefficient is also a function of the aspect ratio of the cylinder, which is not explicitly represented in Eq. (10); hence, strictly speaking, this fit is only applicable to those cases indicated in Table 2. But judging from the smooth behavior of this relation, we feel that it is probably applicable to columnar crystals with dimensions satisfying Auer and Veal's (1970) relations and with flow Reynolds numbers in the aforementioned range. It would be desirable to find a relation of C_D as a function of the aspect ratio. However, more calculations are needed to establish this relation. This is not done for the present study due to the constraint of computing resources.

b. General features of the flow fields around falling hexagonal ice crystals

Pioneering numerical work on the flow fields around falling ice plates were performed by Pitter et al. (1973), who used thin oblate spheroids to approximate planar ice crystals. In the present study, we use the actual hexagonal shape to model the ice plates whose dimensions are given in Table 3. The corresponding range of the Reynolds numbers is from 1 to 120. However, additional cases were also computed as needed to demonstrate the flow fields.

Examples of steady flow fields around hexagonal crystals are shown in Figs. 7 and 8, which represent cases of Reynolds numbers 2 and 20, respectively. These are steady flow cases. The flow fields look similar to those obtained by Pitter et al. (1973).

The flow field of Re = 1 (figure not shown) does not indicate the existence of standing eddies. But there are already standing eddies formed in the wake region of the crystal at Re = 2. This is consistent with Pitter et al. (1973), who indicated that the eddies start to appear at Re = 1.5. As expected, the eddies become larger at higher Reynolds numbers.

Experiments of Willmarth et al. (1964) showed that at $\mathrm{Re} \geq 100$, eddy shedding occurs in the downstream of a falling disk. Such unsteady behavior can be simulated using the same technique as we did for the finite cylinders. Figure 9 shows the simulated unsteady flow fields for flow past hexagonal plates at Re = 140. The initial perturbation introduced (after the steady-state solution has been obtained) was again $0.3\mathbf{V}_\infty$, which has

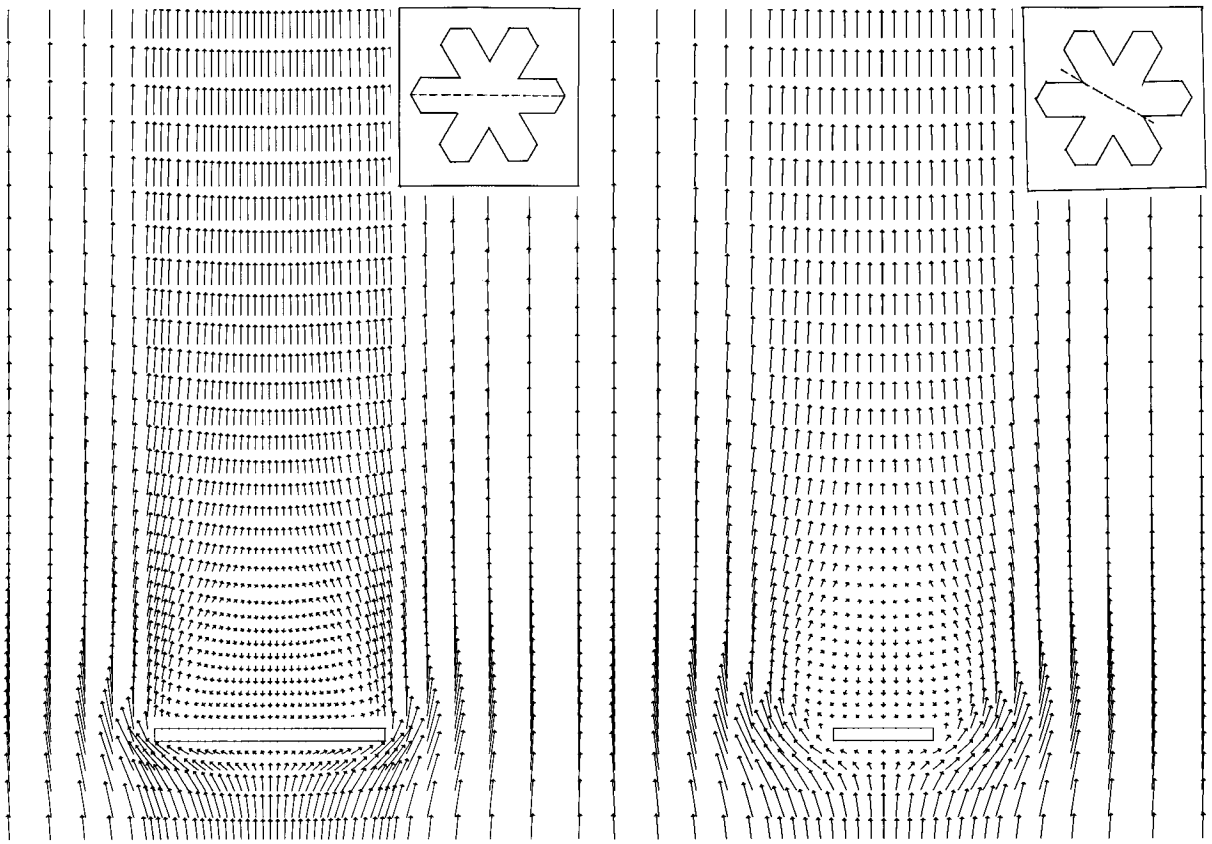

FIG. 11. Velocity fields of flow past a broad-branch ice crystal at Re = 20. The cross-section location is indicated by the dashed line in the upper right corner of the figure.

been proven to be adequate for kicking up the shedding. It can be seen that the flow field is obviously asymmetric due to the shedding. Detailed analysis of how shedding starts has not been done yet, but it is expected that the shedding would start at a particular corner and the point of detachment would rotate around on the plate.

It must be stressed here that the flow fields described above are computed assuming that the plate position is fixed with respect to the incoming air flow; that is, the angle between the c axis (normal to the plate basal surface) of the plate and the general flow is kept at 90°. In reality, falling plates are known to perform zigzag motion, which implies that the angle is not constant but is actually a function of time. In order to simulate such zigzag motions, one has to use very small time steps for adequate accuracy. Due to the constraint of computing resources, these cases are not yet simulated here but are currently being studied by us. However, it is expected that the above results should give good approximations, especially when the variations of the angles are not large.

There seems to be no experimental measurements available for flow properties past hexagonal plates. Willmarth et al.'s (1964) results for flow past circular plates are the closest cases for the comparison purpose. But here the comparison is difficult to make because the aspect ratios of the computed and experimental results are different. For the same reason the comparison between our present results and those of Pitter et al. (1973) is also difficult to make. The aspect ratio of the plates calculated here varies with the Reynolds number, whereas the thin oblate spheroids in Pitter et al. (1973) have fixed aspect ratios ($h/d = 0.05$), and therefore the computed results cannot be compared directly except for the case of Re = 20. At this Re, the drag coefficient obtained by Pitter et al. (1973) agrees with the present result for hexagonal plate to within 1%. Willmarth et al.'s (1964) results do not have the case of Re = 20, and the two cases that are close have rather different aspect ratios ($h/d = 0.0033$ for Re = 15.7 and 0.00167 for Re = 29.1). In other Reynolds number cases, the differences are somewhat larger possibly due to the different aspect ratios (and, of course, somewhat different shapes). But even there, the largest error that occurs at Re = 140 is less than 15%. Thus it seems fair to conclude that the general trend and the magnitude of C_Ds are indeed quite similar for the present and Pitter et al. (1973) cases; hence the predictions made by Pitter et al. (1973) seem to be generally valid.

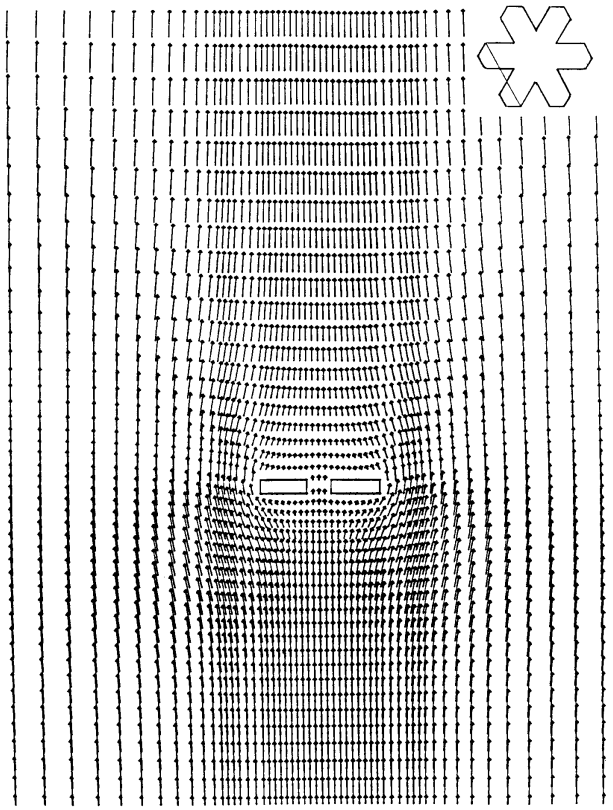

FIG. 12. Velocity field of flow past a branch gap of a broad-branch ice crystal at Re = 2. The cross-section location is indicated by the dashed line in the upper right corner of the figure.

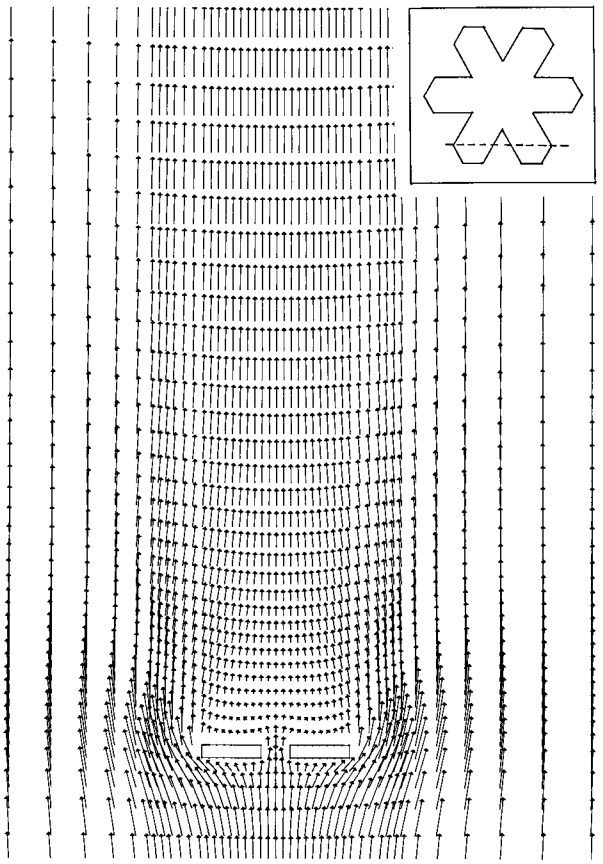

FIG. 13. Velocity field of flow past a branch gap of a broad-branch ice crystal at Re = 20. The cross section is indicated by the dashed line in the upper right corner of the figure.

c. General features of the flow fields around falling broad-branch crystals

Broad-branch crystals are also a common form of ice and snow crystals. We have not seen any quantitative measurements or calculations before about the flow fields around a falling broad-branch crystal, so the present results may be the first of their kind. Needless to say, it would be desirable to have experimental measurements in the future to compare with our computational results.

Because broad-branch crystals are basically planar crystals just like the ice plates discussed in the previous section, the flow fields around them are expected to be similar (albeit different in magnitudes) to that around ice plates. This in indeed the case as shown by the present calculations. The major difference between a plate and a broad-branch crystal, of course, is in the gaps between the branches of the latter. Figures 10 and 11 show the computed flow fields around falling broad-branch crystal for Re = 2.0 and 20, respectively. There are already standing eddies in the flow field of Re = 2.0 although they are so small as to be just barely discernible. The sizes of the eddies are smaller than those for flow past plates at the same Reynolds number. This may be understood by noting that the gaps between branches would allow the fluid to go through more easily and therefore reduce the tendency of creating return flow, which constitutes the eddies.

The flow in the gap region is of particular interest since this phenomenon has never been studied before. Figure 12 shows a special cross section of the flow field that reveals the nature of this regional flow. The flow converges slightly before entering the gap region, becomes relatively straight in the gap, and then diverges slightly upon leaving it. The magnitude of the flow velocity is relatively small.

The standing eddy size again increases with increasing Reynolds number as shown by Fig. 13 for Re = 20. The same covergent–straight–divergent behavior occurs in the gap region, as shown in Fig. 12, only more evident because of the slighter higher velocity than the Re = 2.0 case. However the velocity in this region is still small when compared to the general flow. This generally small velocity phenomenon seems to indicate that the flow in the gap regions can be approximated as creeping flow. If this observation can be substantiated by future studies, then it implies that we can use the creeping flow theory to treat the even more intricate

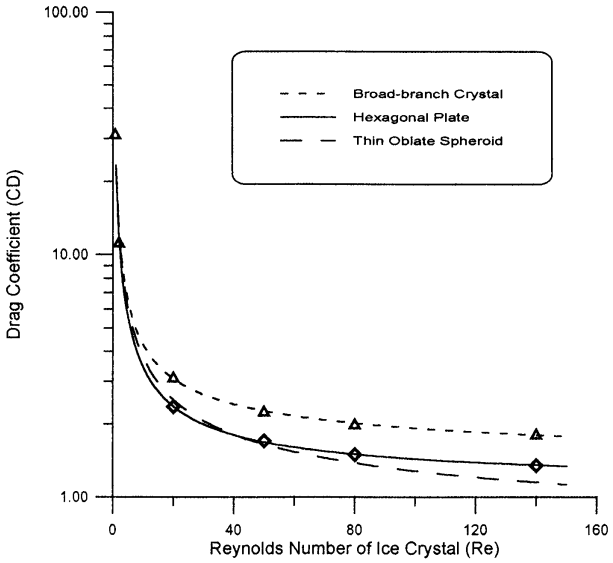

FIG. 14. Drag coefficients as a function of Reynolds number for flow past hexagonal plates and broad-branch crystals.

case of flow going through dendritic crystals where the gaps are even smaller.

Finally, Fig. 14 shows the variation of drag coefficients as a function of Reynolds number for flow around hexagonal plates and broad-branch crystals. The drag coefficient for a broad-branch crystal is greater than that for a plate at the same Reynolds number. The drag coefficients for very thin oblate spheroids as calculated by Pitter et al. (1973) is also plotted for comparison. The drag coefficients for the hexagonal plates and broad-branch crystals computed in the present study can be fitted by the empirical formulas that use the similar functional form as that of Pitter et al. (1973) for circular plates.

Hexagonal plates:

$$C_D = \left(\frac{64}{\pi\ \mathrm{Re}}\right)(1 + 0.078\ \mathrm{Re}^{0.945}) \qquad (12)$$

Broad-branch crystals:

$$C_D = \left(\frac{64}{\pi\ \mathrm{Re}}\right)(1 + 0.142\mathrm{Re}^{0.887}), \qquad (13)$$

which are valid for the range of Re between 0.2 and 150. Both fit the calculated values of drag coefficients to within 1.5%. There are presently no experimental data available to verify the calculations of flow fields for flow past broad-branch crystals.

6. Conclusions

In this study we showed that the unsteady flow fields around three types of falling ice crystals can be determined by numerically solving the time-dependent Navier–Stokes equations. Nonuniform Cartesian grids were used due to the complexity of the crystal geometry, which always results in truly three-dimensional flow fields. Comparisons of present numerical results with experimental data, when available, show good quantitative agreement between the two. This indicates that the present technique is capable of realistically simulating the flow fields around falling ice crystals. This also gives us some confidence of using the computed flow fields to derive other cloud physical quantities that depend strongly on the hydrodynamic effects, such as the collision efficiencies of small particles (cloud droplets, aerosol particles, etc.) with these ice crystals and the ventilation factors that influence the evaporation, cooling, and diffusional growth of these crystals. The computations of these quantities were also performed and will be reported in a later paper.

The present results represent an ongoing attempt to more accurately simulate the flow fields around falling ice crystals and hence are far from perfect. In particular, the ice crystals in the present study are all held fixed with respect the air flow; thus the zigzag motions of some larger crystals are not simulated. We are hoping that this deficiency can be removed in the near future. Considerable computing resource will be necessary for this type of study since the required time step to achieve reasonable accuracy is likely to be rather small. However, judging from the recent impressive advances of computer speed, such computations will probably soon become possible.

What are really lacking are experimental measurements of flow fields around falling ice crystals that are necessary to verify the theoretical results. Ideal equipment for this purpose will be a vertical wind tunnel such as the one used by Mitra et al. (1990). Hopefully, measurements of this kind will become available in the future.

Acknowledgments. This work is partially supported by the NSF Grants ATM-9314465 and ATM-9633424 to the University of Wisconsin–Madison. The senior author (PKW) is also grateful for the support of a Humboldt Award sponsored by the Alexander Humboldt Stiftung—Germany and a S.C. Johnson Distinguished Fellowship to his research group by Johnson Wax, Inc.

REFERENCES

Anderson, D. A., J. C. Tannehill, and R. H. Pletcher, 1984: *Computational Fluid Mechanics and Heat Transfer*. McGraw-Hill, 599 pp.

Auer, H. A., and D. L. Veal, 1970: The dimensions of ice crystals in natural clouds. *J. Atmos. Sci.*, **27,** 919–926.

Braza, M., P. Chassiang, and H. H. Minh, 1986: Numerical study and physical analysis of the pressure and velocity fields in the near wake of a circular cylinder. *J. Fluid Mech.*, **165,** 79–130.

Carrier, G., 1953: On slow viscous flow. Final Rep. Office of Naval Research Contract Nonr-653(00), 31 pp. [Available from Brown University, Providence, RI02912.]

Clift, R., J. R. Grace, and M. E. Weber, 1978: *Bubbles, Drops, and Particles.* Academic Press, 380 pp.

Davis, R. W., 1984: Finite difference methods for fluid flow. *Computational Techniques and Applications,* J. Noye and C. Fletcher, Eds., Elsevier, 51–69.

Dennis, S. C. R., and G. Z. Chang, 1969: Numerical integration of the Navier–Stokes equations for two-dimensional flow. *Phys. Fluid,* Suppl. II, 88–93.

——, and ——, 1970: Numerical solutions for steady flow past a cylinder at Reynolds numbers up to 1000. *J. Fluid Mech.,* **42,** 471–489.

Freitas, C. J., R. L. Street, A. N. Findikakis, and J. R. Koseff, 1985: Numerical simulation of three-dimensional flow in a cavity. *Int. J. Numer. Methods Fluids,* **5,** 561–575.

Goldstein, S., 1929: Forces on a solid body moving through viscous fluid. *Proc. Roy. Soc. London,* **A123,** 216–235.

Hadamard, J., 1911: Mouvement permanent lent d'une sphere liquide et visqueuse dans un liquid visqueux. *Comptes. Rendus.,* **152,** 1735–1738.

Hamielec, A. C., and J. D. Raal, 1969: Numerical studies of viscous flow around a circular cylinder. *Phys. Fluids,* **12,** 11–22.

Happel, J., and H. Brenner, 1965: *Low Reynolds Number Hydrodynamics.* Prentice-Hall, 533 pp.

Jayaweera, K. O. L. F., and B. J. Mason, 1965: The behavior of freely falling cylinders and cones in a viscous fluid. *J. Fluid Mech.,* **22,** 709–720.

Jenson, V. G., 1959: Viscous flow round a sphere at low Reynolds numbers. *Proc. Roy. Soc. London,* **A249,** 346–366.

Ji, W., and P. K. Wang, 1990: Numerical simulation of three-dimensional unsteady viscous flow past fixed hexagonal ice crystals in the air—Preliminary results. *Atmos. Res.,* **25,** 539–557.

——, and ——, 1991: Numerical simulation of three-dimensional unsteady viscous flow past finite cylinders in an unbounded fluid at low intermediate Reynolds numbers. *Theor. Comput. Fluid Dyn.,* **3,** 43–59,

Kovasznay, L. S. G., 1949: Hot wire investigation of the wake behind cylinders at low Reynolds numbers. *Proc. Roy. Soc. London,* **A198,** 174–190.

Lamb, H., 1945: *Hydrodynamics.* Dover, 738 pp.

Le Clair, B. P., A. E. Hamielec, and H. R. Pruppacher, 1970: A numerical study of the drag on a sphere at low and intermediate Reynolds numbers. *J. Atmos. Sci.,* **27,** 308–315.

Leonard, B. P., 1979: Adjusted quadratic upstream algorithms for transient incompressible convection. *A Collection of Technical Papers; AIAA Computational Fluid Dynamics Conference,* AIAA Paper 79-1469.

Masliyah, J. H., and N. Epistein, 1970: Numerical study of steady flow past spheroids. *J. Fluid Mech.,* **44,** 493–512.

Miller, N. L., and P. K. Wang, 1989: A theoretical determination of the efficiency with which aerosol particles are collected by falling columnar ice crystals. *J. Atmos. Sci.,* **46,** 1656–1663.

Mitra, S. K., S. Barth, and H. R. Pruppacher, 1990: A laboratory study of the scavenging of SO2 by snow crystals. *Atmos. Environ.,* **24,** 2307–2312.

Peyret, R., and T. D. Taylor, 1983: *Computational Methods for Fluid Flow.* Springer-Verlag, 358 pp.

Pitter, R. L., 1977: Scavenging efficiency of electrostatically charged thin ice plates and spherical aerosol particles. *J. Atmos. Sci.,* **34,** 1797–1800.

——, H. R. Pruppacher, and A. E. Hamielec, 1973: A numerical study of viscous flow past thin oblate spheroid at low and intermediate Reynolds numbers. *J. Atmos. Sci.,* **30,** 125–134.

——, ——, and ——, 1974: A numerical study of the effect of forced convection on mass transfer from a thin oblate spheroid in air. *J. Atmos. Sci.,* **31,** 1058–1066.

Pruppacher, H. R., and J. D. Klett, 1978: *Microphysics of Clouds and Precipitation.* D. Reidel, 714 pp.

——, B. P. Le Clair, and A. E. Hamielec, 1970: Some relations between the drag and flow pattern of viscous flow past a sphere and a cylinder at low and intermediate Reynolds numbers. *J. Fluid Mech.,* **44,** 781–790.

Rimon, Y., and H. J. Lugt, 1969: Laminar flows past oblate spheroids of various thicknesses. *Phys. Fluids,* **12,** 2465–2472.

Schlamp, R. J., H. R. Pruppacher, and A. E. Hamielec, 1975: A numerical investigation of the efficiency with which simple columnar ice crystals collide with supercooled water drops. *J. Atmos. Sci.,* **32,** 2330–2337.

Takami, H., and H. B. Keller, 1969: Steady two-dimensional viscous flow of an incompressible fluid past a circular cylinder. *Phys. Fluid,* Suppl. II, 51–56.

Thom, A., 1933: The flow past circular cylinders at low speeds. *Proc. Roy. Soc. London,* **A141,** 651.

Willmarth, W. W., N. E. Hawk, and R. L. Harvey, 1964: Steady and unsteady motions and wakes of freely falling disks. *Phys. Fluids,* **7,** 197–208.

Yih, C.-S., 1969: *Fluid Mechanics.* McGraw-Hill, 622 pp.